Sommerfeld Effect Characterisation in Rotors with Non-ideal Drive from Ideal Drive Response and Power Balance

M. Karthikeyan *Alfa Bisoi* *A.K. Samantaray* *R. Bhattacharyya*
Department of Mechanical Engineering, Indian Institute of Technology,Kharagpur, India
mkkeyan@gmail.com, alfabisoi@yahoo.in, samantaray@mech.iitkgp.ernet, rbmail@iitkgp.ernet.in

***Abstract*— Rotor dynamic systems are often analyzed with ideal drive assumption. However, all drives are essentially non-ideal, i.e., they can only provide a limited amount of power and their dynamics is coupled with the driven system's dynamics. One basic fact often ignored in rotor dynamics is that the motor power is not only spent to spin the rotor shaft but also to overcome the resistances to rotation and more importantly, to overcome the power dissipated in lateral vibrations during rotor whirl. Near the resonances, a flexible rotor with unbalance can attain several stable operating speeds for the same amount of input drive power. Increase in power input near resonance may contribute to increasing the transverse vibrations rather than increasing the rotor spin, i.e., the rotor spin may get caught near resonance for considerable range of power input and time. This classic symptom is referred to as the Sommerfeld effect. In this article, we generate the rotor response with finite element (FE) model by assuming an ideal drive. Thereafter, the ideal rotor system's response is used in a power balance equation to theoretically predict the characteristics of the non-ideal system. The non-ideal system with drive-rotor interaction is modeled in bond graph (BG) form whose transient analysis is used to validate the theoretical results. The Sommerfeld effect is studied near the first two critical speeds of the rotor and the passage through resonance conditions are investigated. The results are important from the point of actuator sizing for rotors.**

Keywords: Sommerfeld effect, Non-ideal drive, Rotor dynamics, Finite element model, Bond graph.

I. INTRODUCTION

Sommerfeld effect [1, 2] is observed in eccentric rotor dynamic systems when the input power is increased to bring the shaft speed near a critical speed. When the input power is increased further to increase the shaft speed, the extra input power ends up in exciting the lateral flexural vibrations and the shaft speed does not increase appreciably. This continues till the power input is increased sufficiently whereupon the rotor spin speed suddenly jumps to a much higher value and the transverse vibration amplitudes reduce appreciably. Similar phenomenon is observed during coast down operation, *i.e.*, speed during reduction, where near the critical speed the rotor spin speed jumps from a higher value to a lower value and the flexural amplitudes jump from large values to very small values. One interesting property of Sommerfeld effect is that certain rotor speeds near the critical speeds can never be achieved both during coasting up and down [3]. Sommerfeld effect leads to large synchronous whirl amplitudes during passage through resonance [4, 5]. Previous works in this field have derived closed form solution for Sommerfeld effect in symmetric rotor systems driven by non-ideal source [6] and source interactions at stability threshold [7, 8]. Such works consider Sommerfeld effect at the first critical speed and neglect the gyroscopic coupling. In this work, we present a semi-numerical solution for Sommerfeld effect at higher critical speeds in any general rotor dynamic system with gyroscopic coupling and rotating material damping.

Sommerfeld effect characterization through purely simulation studies is extremely time consuming and requires a great deal of effort due to stiff governing equations. In our approach, we simulate FE model of the corresponding rotor dynamic system with ideal drive to generate its steady-state response characteristics. We use polynomial approximations to represent the steady-state synchronous whirl amplitudes as function of the rotor speed. We then use a bond graph model of the rotor along with its non-ideal drive to balance the power input from the motor with the power dissipated by the system. Use of the response characteristics obtained from the FE simulations of the rotor system with ideal drive in the power balance equation for the non-ideal drive yields predictions of the rotor spin speed(s) and amplitude(s) at any given power supply in the non-ideal system.

II. SOMMERFELD EFFECT CHARACTERIZATION FROM IDEAL DRIVE RESPONSE

A. System Description

A uniform continuous shaft carrying a rigid rotor, as shown in Fig.1, is considered here with simply supported ends or ideal bearings. The rotor is driven by a DC motor which is a non-ideal drive. The shaft has uniform circular cross section and it has no unbalance. The disc is mounted with its plane perpendicular to the shaft axis. The mass center of the rotor disk has an eccentricity e. The torsional vibration of the shaft is neglected. The shaft has internal damping, bearing damping and external transverse and rotary damping act on the rotor disk.

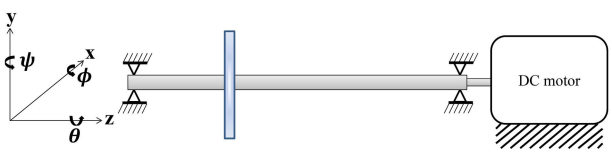

Fig. 1. Continuous shaft with offset disk rotor system driven by a DC motor.

B. *Modal Analysis through Finite Element Model*

Obtaining the critical speeds and stability thresholds through analytical methods is a complex task. As an alternative, FEA is used to study the critical speed and stability threshold. The continuous rotor system is discretized into a finite degrees-of-freedom system and modeled using FE software ANSYS. The shaft is modeled using BEAM188 element and the rigid disk is modeled using MASS21 element. The external translational and rotational dampers are both modeled using a MATRIX27 element which contributes a damping matrix to the node to which it is attached. The coefficients of the damping matrix are the translational and rotational damping coefficients. The internal damping coefficient is specified using the BETAD command. The rotating internal damping, which in the stationary reference frame contributes to the system's stiffness and damping matrices, is modeled using the 'damping effect' option in CORIOLIS command. The stationary reference frame is selected using the 'reference frame' option in CORIOLIS command. The gyroscopic couples and their associated damping forces are also modeled using the 'Coriolis effect' option in the CORIOLIS command. The gyroscopic damping matrices are generated for BEAM188 element and MASS21 element. The unbalance forces on the disk due to its eccentricity are modeled by applying them as nodal forces on the node where the MASS21 element is attached. Refer to ANSYS 13.0 manual for details of commands and elements. A modal analysis of the system is carried out using Q-R damped solver to find the complex eigenvalues of the system.

TABLE I. PARAMETERS, THEIR DESCRIPTIONS AND VALUES.

Parameter	Description	Value	
		Case 1	***Case 2***
E	Young's modulus of shaft material	2×10^{11}Pa	2×10^{11}Pa
ρ	Density of shaft material	7800 kg/m^3	7800 k/m^3
r	Shaft radius	0.0175 m	0.0175 m
L	Shaft length	2 m	2 m
z_d	Position of rotor disk from left bearing end	0.66m	0.66m
M_d	Mass of the disk	110 kg	110 kg
I_d	Polar rotary inertia of disk	3 kgm^2	3 kgm^2
e	Eccentricity in rotor disk	0.001m	0.001m
μ_i	Internal damping parameter in shaft	0.0002 s	0.0002 s
R_t	Direct translational damping coefficient on disk	20 Ns/m	250 Ns/m
R_r	Direct rotational damping coefficient on disk	1 Nms/rad	50 Nm/rad
R_b	Bearing rotational damping coefficient	0.2 Nm/rad	0.2 Nm/rad
V_s	DC motor supply voltage	Variable	Variable
R_m	DC motor electrical armature resistance	5Ω	5Ω
μ_m	DC motor characteristic constant	0.4Nm/A	0.4Nm/A

We have considered two cases to demonstrate the influence of rotor parameter values on the Sommerfeld effect. The two sets of parameter values are given in Table 1. The parameters for rotor eccentricity, bearing and DC motor are not used in FEA; they are used later for non-ideal system simulation using a bond graph model.

In the FE model, the shaft was reticulated to 21 1D beam elements with 22 nodes. The rotor disk was positioned in 15th node. By using FEA technique we obtained the Campbell diagrams for the rotor shaft from which the rotor critical speeds were determined. Also, the stability threshold of the rotor system was obtained.

The real parts of eigenvalues obtained from the modal analysis with the first set of data (Case 1) are plotted in the form of Campbell diagram in Fig. 2. The imaginary parts of the same eigenvalues are shown in Fig. 3. In these figures, labels FW and BW indicate forward and backward whirls, respectively, and the preceding numeral indicates the mode number.

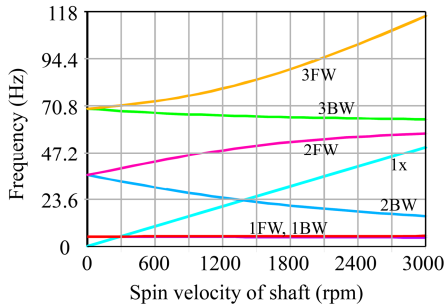

Fig. 2. Campbell diagram showing natural frequency vs. shaft speeds for Case 1 parameters.

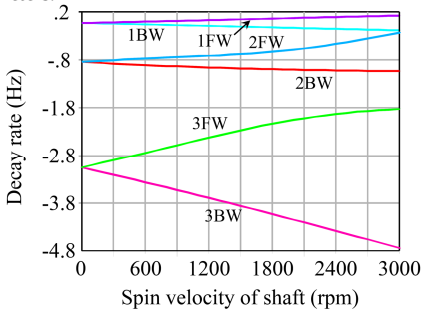

Fig. 3. Campbell diagram showing imaginary part of eigenvalues vs. shaft speed for Case 1 parameters.

As seen from Fig. 3, stability threshold obtained is 567.4 rpm (59.42 rad/s) at which the imaginary part of any (here, 1st mode) eigenvalue (decay rate) becomes positive. The critical speed obtained from Fig. 2 (intersection of 1x line with forward whirl frequencies) is 4.8954 Hz (30.759 rad/s). At the stability threshold, first mode vibrations grow whereas all other mode vibrations remain stable.

Likewise, the real and imaginary parts of eigenvalues obtained from the modal analysis for the second data set (Case 2) are plotted as Campbell diagrams in Figs. 4 and 5, respectively.

The critical speeds in this case are 4.8954 Hz (30.759 rad/s) for first mode and 57.7584 Hz (362.907 rad/s) for second mode. As seen from Fig. 5, the stability threshold is 3838.3 rpm (401.941 rad/s) at which the second mode vibrations become unstable whereas other mode vibrations (including first mode) remain stable.

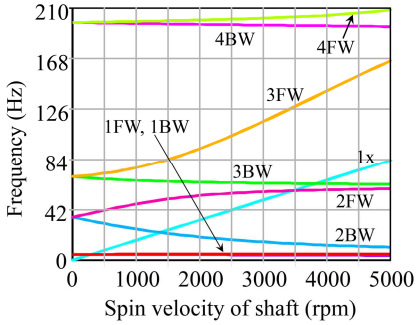

Fig. 4. Campbell diagram showing natural frequency vs. shaft speed for Case 2 parameters.

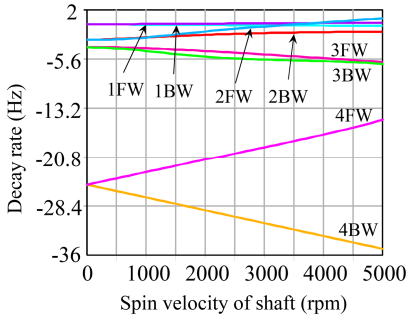

Fig. 5. Campbell diagram showing imaginary part of eigenvalues vs. shaft speed for Case 2 parameters.

C. Sommerfeld effect characterization

In this section the theoretical framework for finding the Sommerfeld effect near the critical speeds is developed. The source loading on the drive due to flexural vibrations can be determined through instantaneous power balance. The same power balance principle was used in some previous works to analyze distributed parameter non-ideal systems [8]. The power dissipated at any instant from a synchronously whirling rotor through the dissipative forces in transverse and rotary vibrations acting on the rotor disk and the bearing damping is given by

$$W_d = R_b\dot{\theta}^2 + R_t\left(\left(\frac{\partial x}{\partial t}\right)^2+\left(\frac{\partial y}{\partial t}\right)^2\right)\Bigg|_{z=2L/3} + R_r\left(\left(\frac{\partial \phi}{\partial t}\right)^2+\left(\frac{\partial \psi}{\partial t}\right)^2\right)\Bigg|_{z=2L/3} \quad (1)$$

where x and y are the transverse displacement of rotor, ϕ and ψ are the rotations about the x and y axes, L is the length of the rotor and z is position along shaft length. Note that the material damping does not contribute to dissipations during synchronous rotor whirl. The rotor disk is positioned at $Z = 2L/3$.

The power generated by the motor is given by

$$W_m = \tau_m\dot{\theta} = \mu_m i_m\dot{\theta} = \mu_m\dot{\theta}\left(V_s - \mu_m\dot{\theta}\right)\Big/R_m \quad (2)$$

Where τ_m is the motor torque, $\dot{\theta}$ is the shaft angular/spin velocity, μ_m is motor characteristic, i_m is the motor current, R_m is the motor armature resistance and V_s is the motor supply voltage. The power transfer mechanism in steady state synchronous whirl [8, 9] can be written as

$$W_m = W_d \quad (3)$$

In order to solve the above equation for power balance, the closed-form analytical expressions for x, y, ϕ and ψ displacements of the rotor must be obtained. Obtaining the response in a closed form for any general multi-disk rotor system is a complex task. Hence an alternative method is considered in this work. In stable operating range, the rotor transverse and rotary displacements reach a steady state value corresponding to the shaft speed. The displacements depend only on the shaft speed and they are independent of the type or nature of the driving system. Hence these displacements can be found by driving the rotor system with an ideal power source at various constant speeds in the region of interest. We reduce the dimension of the problem by considering that near the critical speeds, where the Sommerfeld effect is predominant, most of the power supplied to the rotor system goes to excite a particular mode and the energy in the other modes is negligible in comparison. Considering one mode approximation, the solution for x, y, ϕ and ψ displacements during steady-state synchronous whirl can be considered to be a harmonic temporal form as given below.

$$x(t) = A(\omega)\cos(\omega t+\varphi),\ y(t) = A(\omega)\sin(\omega t+\varphi) \quad (4)$$

$$\phi(t) = B(\omega t)\cos(\omega t+\chi),\ \psi(t) = B(\omega t)\sin(\omega t+\chi) \quad (5)$$

where the amplitudes A and B are functions of the shaft speed, $\omega = \dot{\theta}$, and φ and χ are two phases which are not useful in our study. To obtain $A(\omega)$ and $B(\omega)$, a transient analysis of the ideal power source driven rotor system at constant speed is performed using ANSYS.

Case 1 Result

The transient analysis is used to obtain the transverse and rotational displacement amplitudes in steady state at different constant operating speeds (ideal drive) using the FE model developed in ANSYS. The transverse and rotary whirl amplitudes ($A(\omega)$ and $B(\omega)$) at the rotor (15^{th} node of the FE model) are plotted in Figs. 6 and 7 in the range of the first critical speed.

In order to find an expression to fit the data obtained from ANSYS, a trial function of the following form is assumed for both $A(\omega)$ and $B(\omega)$:

$$T_f(\omega) = \frac{C(1)\omega^2}{\sqrt{C(2)\omega^4 + C(3)\omega^2 + C(4)}} \quad (6)$$

where $C(1), C(2), C(3)$ and $C(4)$ are the coefficients that are to be determined. An objective function, which is the mean square of the error produced between the trial function and the actual response is defined as

$$O(x) = \sum_{i=1}^{n}\left(x(i) - T_f(i)\right)^2 \quad (7)$$

where n denotes the total number of data points obtained using ANSYS and i is the variable that enumerates the data points. A minimization of the objective function is carried out using MATLAB with appropriate initial guess values chosen for the coefficients.

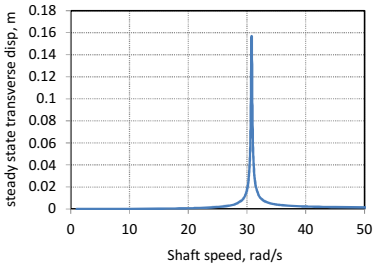

Fig. 6. Steady state transverse displacement vs. shaft speed obtained from ANSYS for case 1 data.

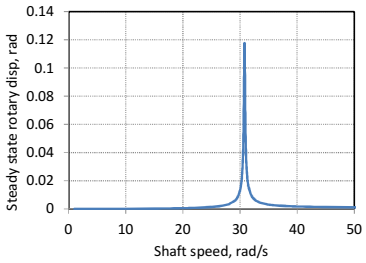

Fig. 7. Steady state rotary displacement vs. shaft speed obtained from ANSYS for case 1 data.

The optimized functions for the steady state transverse and rotary displacements that fit the actual data points within an error of 1×10^{-8} are, respectively, given by

$$A(\omega) = \frac{6.66503336489138\ \omega^2}{\sqrt{51122911\omega^4 - 96871808791\omega^2 + 4589.1\times10^9}} \quad (8)$$

$$B(\omega) = \frac{0.00000295723\ \omega^2}{\sqrt{0.0000179156\omega^4 - 0.03394805566\omega^2 + 16.08324}} \quad (9)$$

Substituting the expression for $A(\omega)$ and $B(\omega)$, in the power balance equation $W_m = W_d$ and simplifying the expression we get the following equation with the supply voltage V_s as a variable parameter.

$$V_s \times 10^{24}(-1.83\omega^8 + 6.94\times10^3\omega^6 - 9.87\times10^6\omega^4 + 6.232\times10^9\omega^2 - 1.48\times10^{12}) + 5.31\times10^{24}\omega^9 - 2.013\times10^{28}\omega^7 + 2.86\times10^{31}\omega^5 - 1.81\times10^{34}\omega^3 + 4.280694\times10^{36}\omega \quad (10)$$

We use the above polynomial to define a transfer function between a fictitious input-output pair as follows.

$$G(s) = \frac{N(s)}{D(s)} = \frac{-1.83\omega^8 + 6.94\times10^3\omega^6 - 9.87\times10^6\omega^4 + 6.23\times10^9\omega^2 - 1.48\times10^{12}}{5.31\omega^9 - 2.01\times10^4\omega^7 + 2.86\times10^6\omega^5 - 1.80\times10^{10}\omega^3 + 4.28\times10^{12}\omega} \quad (11)$$

where s is the Laplace variable (representing ω), $N(s)$ and $D(s)$ are two polynomials in s and V_s is a gain parameter so that the characteristic polynomial $D(s) + V_s N(s)$ turns out to be same as Eq. (11). Now a root locus can be used to study the roots of the characteristic equation $D(s) + V_s N(s) = 0$. In the root loci given in Fig. 8, there is a break-in point at 94V with frequency 31.8rad/s and another break-in point at 111V with frequency 30.8 rad/s. There is a break-away point at 145V with frequency 30.7rad/s. Till 94V, there is only branch of solution on real axis which means there is only one positive real root of Eq. (10). From 94V to 111V, there are three branches of solutions on real axis which means there are three positive real roots. These roots indicate three possible shaft spin speeds at a given constant input voltage. Out of the three, two are stable solutions and one is unstable. These stability conditions are detailed in [6]. From 111V to 145V, five branches of root loci lie on the real axis which means there are 5 possible rotor spin speeds for a motor supply voltage within the specified range. Of these, three are stable roots and two are unstable. For $V_s < 94$V and $V_s > 145$V , only one positive real root exists; which means the rotor has a unique operating speed for a given motor supply voltage.

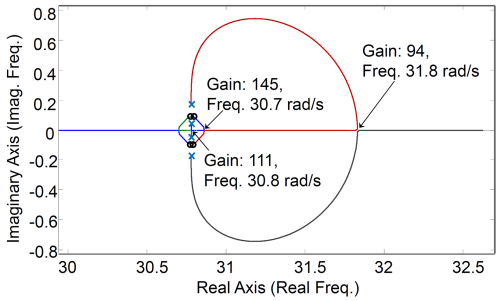

Fig.8. Root locus to determine shaft spin speeds near first critical speed for various motor supply voltages.

The same results are shown in Figure 9 with the area around the Sommerfeld effect zoomed in Fig. 10. In these figures, only the real positive shaft spin speeds are plotted. For the Case 1 data set, the Sommerfeld effect near the 2nd critical speed is so severe that it requires a huge value of input voltage to overcome it. Moreover, the 2nd critical speed is near the stability threshold and it is therefore not suitable to operate a rotor in that regime. Other critical speeds are above the stability threshold and are thus not considered.

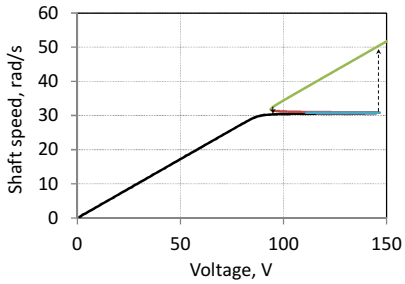

Fig. 9. Shaft speed vs. voltage for case 1 data.

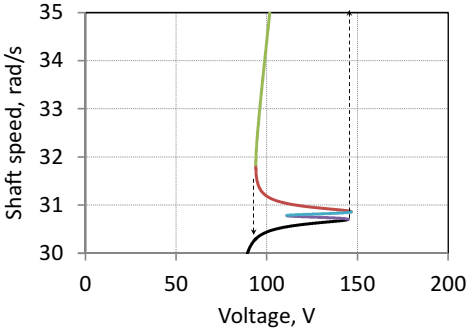

Fig. 10. Enlarged view of Fig. 9.

Case 2 Result

When the second set of data is used, by using the method followed just before, we found that there is no Sommerfeld near the first critical speed, i.e., for all values of supply voltage required to drive the system through the first critical speed there is a unique rotor spin frequency. The disappearance of Sommerfeld effect in the first mode is due to the large values of external damping acting on the disk. This effect has been detailed in [6].

ANSYS was used to obtain the steady-state transient response of the system near the second critical speed. The transverse and rotary displacement amplitudes in the range of the second critical speed are plotted in Figs. 11 and 12, respectively. Like earlier case, here we assume that most of the energy supplied by the motor goes to excite the second mode vibrations.

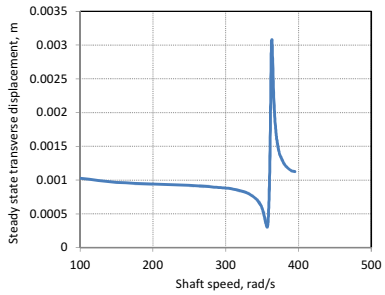

Fig. 11. Steady state transverse displacement vs. shaft speed obtained from ANSYS for case 2 data.

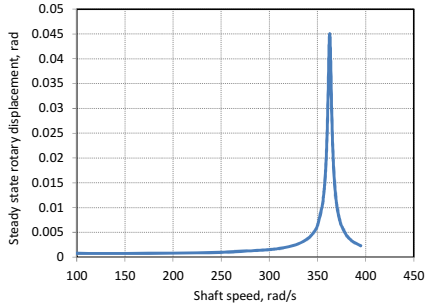

Fig. 12. Steady state rotary displacement vs. shaft speed obtained from ANSYS for case 2 data.

For data fitting, the trial function of the following form is assumed for $A(\omega)$

$$T_f = \frac{C(1)\omega^3 + C(5)\omega^2}{\sqrt{C(2)\omega^4 + C(3)\omega^2 + C(4)}} \tag{12}$$

Using MATLAB for least square fitting, the steady state transverse displacement can be approximated by

$$A(\omega) = \frac{0.477921\ \omega^3 - 170.08968\ \omega^2}{\sqrt{11482377770\omega^4 - 3022.6135\times10^{12}\omega^2 + 19893870.7\times10^{13}}} \tag{13}$$

Note that this approximation is valid only when the operating speed is in the neighborhood of the second critical speed. Further note that the trial function has to be suitably chosen to minimize the error. Likewise, the trial function assumed for $B(\omega)$ is given as and the rotary vibration amplitudes in the neighborhood of second critical speed are expressed as

$$T_f(\omega) = \frac{C(1)\omega^2}{\sqrt{C(2)\omega^4 + C(3)\omega^2 + C(4)}} \tag{14}$$

$$B(\omega) = \frac{0.995675928267296\ \omega^2}{\sqrt{5041391\omega^4 - 132600\times10^5\omega^2 + 872007\times10^{11}}} \tag{15}$$

Substituting the expression for $A(\omega)$ and $B(\omega)$in the power balance equation $W_m = W_d$ and simplifying the expression we get the following equation with the supply voltage V_s as a variable parameter.

$$\begin{aligned}&(-2.89\times10^{35}\omega^8 + 1.5232\times10^{41}\omega^6 - 3.0061\times10^{46}\omega^4 \\ &+2.64\times10^{51}\omega^2 - 8.674\times10^{55})\times V_s + 1.799\times10^{28}\omega^{11} \\ &-1.280\times10^{31}\omega^{10} + 8.369\times10^{35}\omega^9 + 3.368\times10^{36}\omega^8 \\ &-4.4202\times10^{41}\omega^7 - 2.2152\times10^{41}\omega^6 + 8.722\times10^{46}\omega^5 \\ &-7.6468\times10^{51}\omega^3 + 2.5154\times10^{56}\omega\end{aligned} \tag{16}$$

We use the above polynomial to define a transfer function between a fictitious input-output pair as

$$\begin{aligned}G(s) &= N(s)/D(s) \\ &= \frac{\begin{aligned}&-2.89\times10^{35}\omega^8 + 1.5232\times10^{41}\omega^6 - 3.0061\times10^{46}\omega^4 \\ &+2.64\times10^{51}\omega^2 - 8.674\times10^{55}\end{aligned}}{\begin{aligned}&1.799\times10^{28}\omega^{11} - 1.280\times10^{31}\omega^{10} + 8.369\times10^{35}\omega^9 \\ &+3.368\times10^{36}\omega^8 - 4.4202\times10^{41}\omega^7 - 2.2152\times10^{41}\omega^6 \\ &+8.722\times10^{46}\omega^5 - 7.6468\times10^{51}\omega^3 + 2.5154\times10^{56}\omega\end{aligned}}\end{aligned} \tag{17}$$

with V_s as the gain parameter. The roots of the characteristic equation $D(s) + V_s * N(s) = 0$ are shown in the root loci given in Fig. 13.

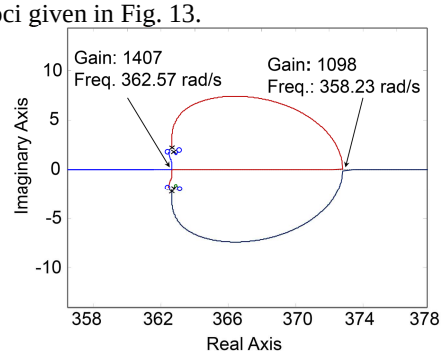

Fig. 13. Root locus to determine shaft spin speeds near second critical speed for various motor supply voltages.

In the root loci given in Fig 13, there is one break-in point at 1098.72V with frequency 358.23rad/s and a break-away point at 1407V with frequency 362.57 rad/s. Till 1098.71V, there is only branch of solution on real axis which means there is only one possible rotor speed for a given supply voltage. The same is true for $V_s > 1407$V. Between 1098.72V to 1407V, there are 3 branches on real axis which means there are 3 possible rotor spin speeds for a given supply voltage in this range. Of these, two are stable solutions and one is unstable. These results are shown in Figure 14 with the area around the Sommerfeld effect zoomed in the inset.

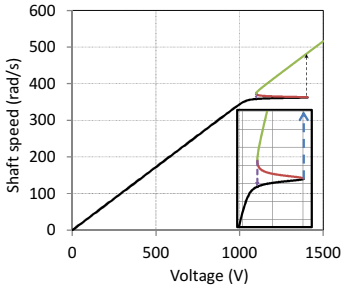

Fig.14. Shaft speed vs. supply voltage for case 2 data.

III. TRANSIENT ANALYSIS OF NON-IDEAL SYSTEM

ANSYS and other FE software do not support transient analysis of rotor dynamic systems with source-loading, i.e., non-ideal drives. Therefore, we seek alternative modeling approach for the system. Because we are looking at energetic consistency in the system model, we use bond graph modeling. A bond graph (BG) model naturally represents consistent power balance across sub-system boundaries [10, 11]. We developed a one-dimensional finite element bond graph model of the rotor system with lumped parameters. The bond graph model automatically incorporates appropriate reactions on the drive and the drive dynamics gets coupled to the rotor dynamics. The multi-energy domain coupling of the electrical DC motor to the mechanical rotor-dynamic system is elegantly represented in a bond graph form. However, it may be noted that modal analysis is more conveniently performed using ANSYS than bond graph tool. Here, we use both FE and bond graph models and integrate both the approaches taking advantage of both the methods.

A. *Bond graph model of the system*

To correctly obtain the natural frequencies, a bond graph model based on Euler-Bernoulli beam theory requires too many elements and the model becomes computationally inefficient. Therefore, we have developed a Raleigh beam model of the rotor shaft by including the diametral rotary inertias, gyroscopic moments and rotating material damping in the model.

The shear force and bending moments developed in a beam element are dependent on both the transverse and the rotary displacements at two ends of the element. The elastic forces in the x-z plane and y-z plane are given by [12]

$$\begin{aligned}
&\begin{pmatrix} V_{xL} & M_{yL} & V_{xR} & M_{yR} \end{pmatrix}^T = \frac{EI}{L^3}\mathbf{K}\begin{pmatrix} x_L & \psi_L & x_R & \psi_R \end{pmatrix}^T \\
&\begin{pmatrix} V_{xL} & -M_{yL} & V_{xR} & -M_{yR} \end{pmatrix}^T = \frac{EI}{L^3}\mathbf{K}\begin{pmatrix} y_L & -\phi_L & y_R & -\phi_R \end{pmatrix}^T \\
&\text{where } \mathbf{K} = \begin{bmatrix} 12 & 6L & -12 & 6L \\ 6L & 4L^2 & -6L & 2L^2 \\ -12 & -6L & 12 & -6L \\ 6L & 2L^2 & -6L & 4L^2 \end{bmatrix}
\end{aligned} \tag{18}$$

where V and M denote shear force and bending moment, respectively, x and y are the transverse displacements along the respective directions, ϕ and ψ denote the rotations along x and y directions, respectively, and subscripts L and R denote the left and the right ends, respectively.

When material damping is considered, the rates of the displacements also influence the shear force and bending moments. The beam internal damping generates forces and moments due to strain rates. It is modeled in a rotating frame whose z-axis is coincident with that of the fixed frame [8, 12]. The damping forces in the rotating frame are given by

$$\begin{aligned}
&\left(\begin{pmatrix} V_{xL} & M_{yL} & V_{xR} & M_{yR} \end{pmatrix}_d^T\right)_r^T = \frac{\mu_i EI}{L^3}\mathbf{K}\begin{pmatrix} \dot{x}_L & \dot{\psi}_L & \dot{x}_R & \dot{\psi}_R \end{pmatrix}_r^T \\
&\left(\begin{pmatrix} V_{xL} & -M_{yL} & V_{xR} & -M_{yR} \end{pmatrix}_d^T\right)_r^T = \frac{\mu_i EI}{L^3}\mathbf{K}\begin{pmatrix} \dot{y}_L & -\dot{\phi}_L & \dot{y}_R & -\dot{\phi}_R \end{pmatrix}_r^T
\end{aligned} \tag{19}$$

where internal damping parameter μ_i is a material constant, subscript d denotes damping, and subscript r indicates that the values are in the rotating frame. The frame transformation of forces and velocities are given by

$$\begin{aligned}
&\begin{pmatrix} (V_x)_d \\ (V_y)_d \end{pmatrix}_f = \begin{pmatrix} \cos\theta & \sin\theta \\ -\sin\theta & \cos\theta \end{pmatrix}\begin{pmatrix} (V_x)_d \\ (V_y)_d \end{pmatrix}_r \\
&\begin{pmatrix} \dot{x} \\ \dot{y} \end{pmatrix}_r = \begin{pmatrix} \cos\theta & \sin\theta \\ -\sin\theta & \cos\theta \end{pmatrix}\begin{pmatrix} \dot{x} \\ \dot{y} \end{pmatrix}_f + \dot{\theta}\begin{pmatrix} -\sin\theta & \cos\theta \\ -\cos\theta & -\sin\theta \end{pmatrix}\begin{pmatrix} x \\ y \end{pmatrix}_f
\end{aligned} \tag{20}$$

where $\theta = \int \omega dt$ is the angle between the fixed and the rotating frames measured about the z-axis. The rotational velocities and moments are likewise transformed using the same transformation formulae.

The bond graph model of the rotor system is developed with 21 one-dimensional finite elements. We develop sub-models for different parts of the model and assemble them to obtain the integrated model.

- Shaft sub-model

The shaft segment models the stiffness and damping of the shaft element. A C-field and an R-field are used to model Eq. (18) and (19) in Fig. 15. A bond with a circle over it indicates a vector bond of dimension 5. These vector bonds are split into scalar bonds and *vice versa* through demux and mux elements indicated by thick vertical lines. The four transformers with moduli -1 implement the negative signs in the expressions for bending moments (M_x) and rotations (ϕ) about the x-axis.

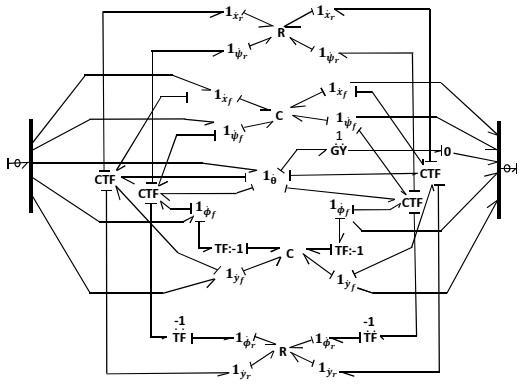

Fig. 15. Bond graph sub-model of a shaft segment.

The CTF block models the coordinate transformations. This block detailed in Fig. 16 implements a transformer junction structure, which being power conservative simultaneously models both force and velocity transformations. Moreover, it generates the source loading through bonds connected to $1_{\dot{\theta}}$ junction in Fig. 16.

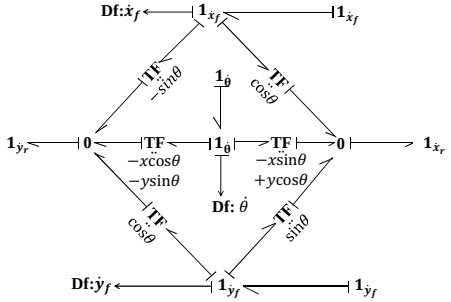

Fig. 16. Linear and angular velocity (force and moment) transformation sub-model.

- Hub sub-model

This models the inertia of the shaft element, which is equivalent to the nodes of the FE model. The four I elements in Fig. 17 model the nodal masses (M) and rotary inertias ($J_{ds} = J_{ps}/2$), where J_{ps} is the polar moment of inertia of the shaft segment. Also, the gyroscopic coupling between the rotations is modeled by using a gyrator. The R elements in the model implement distributed external damping (R_a) which are absent in the present study.

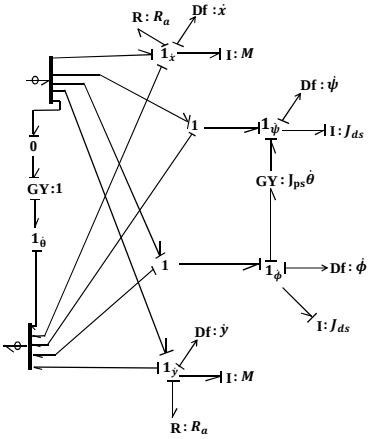

Fig. 17. Bond graph sub-model of the hub element.

- Disk sub-model

This models the rotor disk. It is an extension of the hub sub-model and includes the additional inertia due to the rotor. Also, the eccentricity of the rotor is modeled here. The mass centre and geometric centre of the disk are shown in Fig. 18, where e is the eccentricity and δ is an arbitray initial phase.

The position of the mass center (x_m, y_m) can be expressed in terms of the position and rotation around the geometric center (x, y) as follows:

$$x_m = x + e\cos(\theta + \delta),\ y_m = y + e\sin(\theta + \delta) \quad (21)$$

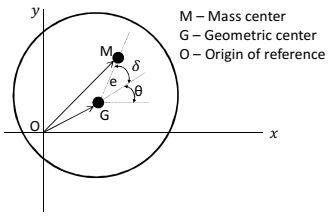

Fig. 18. Shaft cross section showing mass centre and geometric centre.

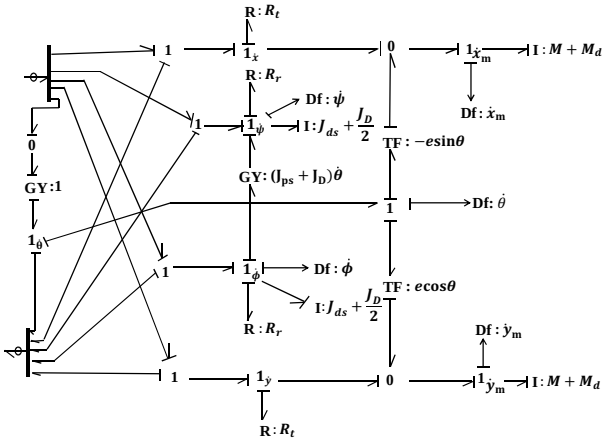

Fig. 19. Bond graph sub-model of the rotor disk.

- Integrated model

The rotor system model with offset disk, boundary conditions and the DC motor drive connected to the left end is shown in Fig. 20.

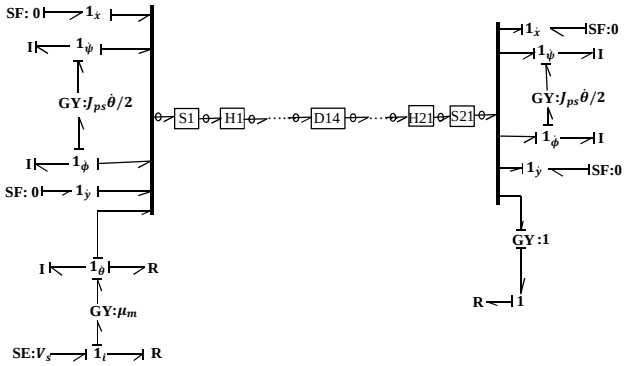

Fig. 20. Bond graph model of the integrated rotor system with DC motor drive.

The ideal pin-pin supports are modeled with zero flow sources on transverse velocities. For free rotations about the pins, half of shaft element rotary inertia is considered at the ends. The R element on the right boundary condition model indicates right bearing damping. The motor supply voltage is modeled by Se element which is connected to a 1-junction where the R element models armature resistance and GY element models DC motor characteristics. In the 1 junction on the other side of the GY element, the I element models total polar moment of inertia of the rotor shaft system (the torsional vibrations have been neglected in this model) and the R element models left bearing damping. The blocks S1, S2 … model shaft segments, H1, H2 … model hubs, and D14 models the rotor disk.

B. *Simulation Results*

To study Sommerfeld effect near the critical speeds, numerical simulations were carried out using the developed bond graph model. The model parameters are already given in Table 1. Additional parameters used in bond graph are motor characteristic, motor resistance, bearing resistance. The model was validated by comparing the results to those from the FE model. For ideal drive simulation, the motor model was replaced by a constant source of flow (SF:ω). The natural frequencies of the rotor system at any given spin speed was obtained by giving arbitrary initial conditions to the disk and then taking the FFT of the response. The natural frequencies from the bond graph model closely matched those from the FE model and also the stability threshold was found to be the same. The validated model is then used to study Sommerfeld effect with the full DC motor model.

Case 1 Simulation

The simulation is done to validate the results plotted in Figs. 9 and 10 which reveal that the range of speed between 30.6288 rad/s and 31.7665 rad/s near the first critical speed cannot be achieved. The non-dimensional variables used to plot the results are $\alpha = 2\omega_1^2\sqrt{x^2+y^2}/(\pi^2 g)$, $\beta = 1.5\pi^2\sqrt{\phi^2+\psi^2}$, and $\gamma = \dot{\theta}/\omega_1$, where ω_1 is the first critical speed and g is the acceleration due to gravity. In the coasting up simulation shown in Fig 21, it can be seen that the shaft speed is caught at the critical speed ($\gamma \cong 1$) due to insufficient supply voltage (V_s =137V) and this gives rise to large amplitude displacements. The results shown in Fig. 22 are for supply voltage V_s =137.1V, where it can be seen that the displacements reach a peak value near the critical speed and then reduce to lower value after the shaft speed escapes the Sommerfeld effect and jumps from the critical speed to a higher value. The simulations show jump during coasting up operation at V_s =137V whereas the theoretically predicted jump voltage was V_s =145V (Fig. 10).

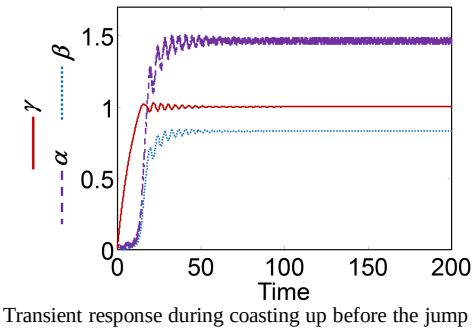

Fig. 21. Transient response during coasting up before the jump for case 1 data.

During coasting down, the jump was predicted at V_s =94V (Fig. 10) whereas simulations show jump at 93V (results not shown). The discrepancies can be attributed to the steady-state assumptions during the theoretical formulations. The results tend to match when the motor supply voltage is quasi-statically varied. However, it is very time consuming and those results are not reported here.

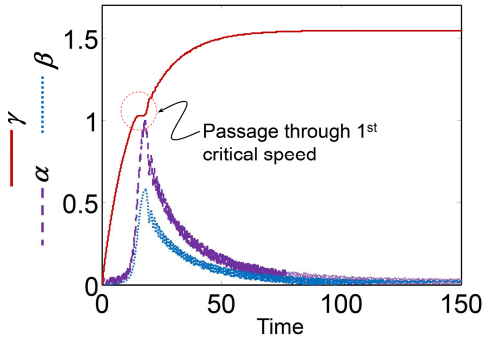

Fig. 22. Transient response during coasting up after the jump for case 1 data.

The Sommerfeld effect characterization obtained from simulations is shown in Fig. 23, which is close to the theoretically predicted characteristics given in Figs. 9 and 10. However, the unstable braches shown in Figs. 9 and 10 cannot be obtained through simulations.

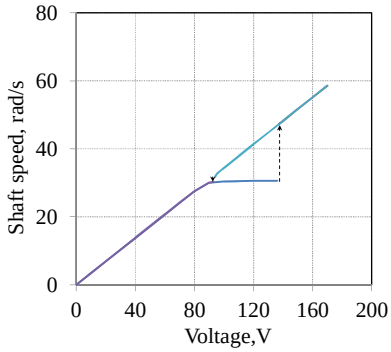

Fig. 23. Shaft speed vs. voltage graph showing both coasting up and coasting down operation

Case 2 Simulation

The simulation is done for range of voltages to obtain shaft speeds in the vicinity of second critical speed. The non-dimensional variables used to plot the results are $\alpha = 0.8\omega_2^2\sqrt{x^2+y^2}/(\pi^2 g)$, $\beta = 1.5\pi^2\sqrt{\phi^2+\psi^2}$, and $\gamma = \dot{\theta}/\omega_2$, where ω_2 is the second critical speed and g is the acceleration due to gravity. The results in Fig. 24 are shown for V_s =1497.5V where the rotor spin speed gets caught at second critical speed $\gamma = 1$. The results do not show steady final values because the second critical speed is very close to the stability threshold speed and thus the decay rate is very small (transients persist).

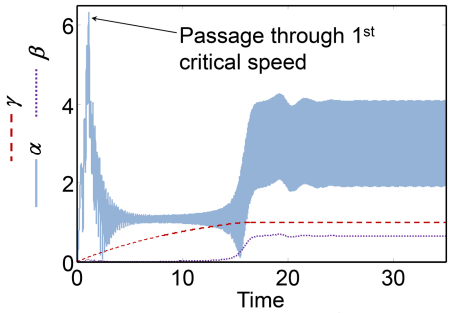

Fig. 24. Transient response during Coasting up before the jump for case 2 data.

The results in Fig. 25 are for V_s =1497.5V which shows escape from the Sommerfeld effect at the second critical speed. However, after escape, the spin speed is caught at the stability threshold speed [6, 8]. Note that in a non-ideal system with limited input power, the vibration amplitudes are finite even when the system is unstable [8]. The supply voltage at which jump is predicted from theoretical analysis is V_s =1407.5V. The simulation shows jump at V_s =1092V during coast down operation whereas the theoretical predictions give the jump at V_s =1098.72V. The error may be attributed to neglecting the eccentricity effect during calculation of rotary inertias.

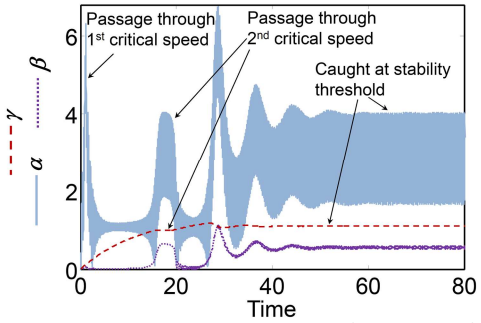

Fig. 25. Transient response during Coasting up after the jump for case 2 data.

The composite figure showing Sommerfeld effect characterization from simulations (with missing unstable branches) is shown in Fig. 26.

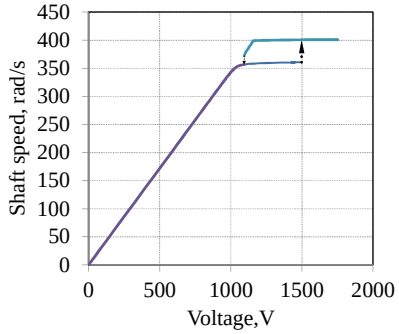

Fig. 26. Shaft speed vs. voltage graph showing both coasting up and coasting down operation for case 2 data.

CONCLUSIONS

We have predicted the Sommerfeld effect characteristics near critical speeds in a continuous shaft with offset disk eccentric rotor system driven through a DC motor by using a semi-analytical method which combines FE model modal analysis with input-dissipation power balance constraint. This is computationally very efficient and can be applied to any general rotor dynamic system with multiple disks. The semi-analytical approach predicts both the rotor spin speed and vibration amplitudes during coasting up and down operations for any given motor supply voltage (or torque). The results have been validated through transient analysis performed with aid of a bond graph model. The transient analysis gives maximum vibration amplitudes reached during the passage through critical speeds.

The prediction of Sommerfeld effect characteristics is very important from the point of view of actuator sizing in a rotor dynamic system designed to operate in super-critical region. One can *a priori* decide on the required motor power and its other ratings needed to drive the rotor through the resonance for a given maximum allowable eccentricity. On the other hand, if the motor specifications are known then one can determine the maximum allowable eccentricity and specify it for rotor balancing.

REFERENCES

[1] A. Sommerfeld, Beiträge Zum Dynamischen Ausbau Der Festigkeitslehe, *Physikal Zeitschr*, 3 (1902), pp. 266–286.

[2] A. Nayfeh, D. Mook, *Nonlinear Oscillations*, Wiley-Interscience, NY (1979).

[3] J.M. Balthazar, D.T. Mook, H.I. Weber, R.M.L.R.F. Brasil, A. Fenili, D. Belato, J.L.P. Felix, An Overview on Non-Ideal Vibrations, *Meccanica*, 38 (2003), pp. 613–621.

[4] M.F. Dimentberg, L. McGovern, R.L. Norton, J. Chapdelaine, R. Harrison, Dynamics of an unbalanced shaft interacting with a limited power supply, *Nonlinear Dyn.*, 13 (1997), pp. 171–187.

[5] A. Ryzhik, T. Amer, H. Duckstein, L. Sperling, Zum Sommerfeldeffect beim selbsttätigen Auswuchten in einer Ebene, *Technische Mechanik*, 21 (4) (2001), pp. 297–312.

[6] A.K. Samantaray, S.S. Dasgupta, R. Bhattacharyya, Sommerfeld effect in rotationally symmetric planar dynamical systems, *Int. J. Engg. Sc.* 48 (1) (2010), pp. 21–36.

[7] A.K. Samantaray, Steady-state dynamics of a non-ideal rotor with internal damping and gyroscopic effects, *Nonlinear Dyn.*, 56 (4) (2009), pp. 443–451.

[8] A.K. Samantaray, S.S. Dasgupta, R. Bhattacharyya, Bond graph modeling of an internally damped nonideal flexible spinning shaft, *J. Dyn. Syst., Meas. and Cont., Trans. ASME* 132 (6) (2010), art. no. 061502.

[9] A.K. Samantaray, On the non-linear phenomena due to source loading in rotor-motor systems, *Proc. IMechE Part-C: J. Mech. Engg. Sc.*, 2009a, 223(4), pp. 809–818.

[10] D.C. Karnopp, D.L. Margolis, R.C.Rosenberg, *System Dynamics: Modeling and Simulation of Mechatronic Systems*, John Wiley & Sons Inc. (2006).

[11] A. Mukherjee, R. Karmakar, A.K. Samantaray, *Bond graph in modeling, simulation and fault identification*, CRC Press, FL (2012).